A. Abbà, A. Recanati, M. Tugnoli, L. Bonaventura
Dynamical p−Adaptivity for LES of Compressible Flows in a High order DG Framework
Journal of Computational Physics, Vol. 420, 2020, 109720 (21 pages)
doi:10.1016/j.jcp.2020.109720

Dynamical $p-$adaptivity for LES of compressible flows in a high order DG framework

Antonella Abbà Alessandro Recanati Matteo Tugnoli

Dipartimento di Scienze e Tecnologie Aerospaziali, Politecnico di Milano
Via La Masa 34, 20156 Milano, Italy

Luca Bonaventura

MOX – Modelling and Scientific Computing,
Dipartimento di Matematica, Politecnico di Milano
Piazza Leonardo da Vinci, 20133 Milano, Italy

Abstract

We investigate the possibility of reducing the computational burden of LES configurations by employing locally and dynamically adaptive polynomial degrees in the framework of a high order DG method. A degree adaptation technique especially featured to be effective for LES applications, that was previously developed by the authors and tested in the statically adaptive case, is applied here in a dynamically adaptive fashion. In this first study, no dynamic load balancing was carried out. Two significant benchmarks are considered, comparing the results of adaptive and non adaptive simulations. The proposed dynamically adaptive approach allows for a significant reduction of the computational cost of representative LES computation, while allowing to maintain the level of accuracy guaranteed by LES carried out with constant, maximum polynomial degree values.

*Antonella Abbà
Email addresses: antonella.abba@polimi.it (Antonella Abbà Alessandro Recanati Matteo Tugnoli), luca.bonaventura@polimi.it (Luca Bonaventura)

1. Introduction

During the last decades, Large Eddy Simulation (LES) has been extensively studied and has achieved results comparable to those of Direct Numerical Simulations (DNS) with a significant reduction in computational cost, enabling the use of high accuracy models to simulate turbulent flows beyond the extremely idealized configurations to which DNS was typically limited. However, in spite of the increase of the available computing power, LES simulations are still computationally very expensive, due to their space and time resolution requirements [1]. Furthermore, selecting the optimal spatial resolution for the LES of an unsteady turbulent flow in a complex geometry is not an easy task [2].

On the one hand, the resolution must be sufficient to solve the equations with adequate accuracy, but limited to contain the computational costs. On the other hand, there is a complex interplay between the effects of numerical diffusion and those of the models used to describe the subgrid scale features. Indeed, some approaches like implicit LES (ILES) methods [3], [4] use the discretization as filter, so that the mesh resolution sets implicitly the filter width and the threshold between the resolved scales and the modelled ones. An early empirical investigation of this issue in the LES framework was presented in [5], which concluded that the LES filter width should be larger than the mesh size. Similar findings were also reported in [6], [7] and related works, based on more sophisticated analysis techniques. ILES methods based on TVD shock-capturing finite volume approaches were studied in [8] and found to introduce excessive numerical diffusion. Several approaches to address these issue and provide grid independent LES have been reviewed in [9]. In [10] it was found that, when high-order numerical dissipation is used, the transfer function associated with the filtering effect is effective in reducing the number of degrees of freedom of the problem, advocating a strategy that introduced both physical and numerical dissipation exclusively in the viscous term. An interesting novel approach for the analysis of the interaction between numerical diffusion and small scale flow structures, based on spatial eigensolutions, has been proposed in [11], [12].

An exhaustive discussion on this aspect is beyond the scope of our work, where the implicit assumption is made that the numerical methods employed are able to reduce the impact of numerical diffusion below that of the LES models at sufficiently high resolution.

In a turbulent flow in complex geometry, turbulence characteristics also change in time and in space throughout the computational domain and cannot be as easily estimated as it was the case in the simple geometries used for many years in LES studies. Therefore, an adaptive LES, able to adapt automatically the resolution and the filter width to the flow conditions, would be of great benefit for the solution of both problems, in order to have an LES with the correct filter sizing and an efficient spatial discretization. However, estimates of the right resolution are further complicated by the fact that, as pointed out by the authors in [13], using estimators only targeted at the reduction of the discretization error are not optimal for LES, if refinement to DNS resolutions is to be avoided, so that specific, physically based strategies must be devised in this context.

The need of an adaptive LES was first stated by [2], but not many attempts have been made in this direction since then. In the numerical solution of PDEs, however, in the last decades considerable efforts have been devoted to the development of refinement indicators. Most of these are based on local estimates of the discretization error, see e.g. [14, 15, 16, 17, 18, 19, 20, 21, 22, 23, 24]. In [25], an indicator based on an estimate of the local regularity of the solution was proposed. Other, more physically based indicators have been proposed and tested, among others, in [26, 27], while a combination of geometrical and physically based indicators was proposed in [28] for free surface flow simulations. In [29], a super-convergent post-processed solution was employed to build a local error indicator. In the LES context, however, simply increasing the resolution in order to decrease the error leads to a DNS solution [30, 31], which is in contrast with the goal of adaptive LES, that consists in adjusting the resolution in order to directly resolve only a prescribed amount of the turbulent scales. In some approaches, presented e.g. in [32, 33, 34, 35, 36], indicators aimed at obtain-

ing a good representation of some quantity of interest are used to adapt the mesh via adjoint and duality-based a posteriori error estimators, which however entail significant computational costs. Comparisons of different $p-$refinement approaches have been carried out in [37, 38, 39].

In the present work, we will consider the physically based refinement indicator proposed by the authors in [13, 40], which is especially suited for LES. This adaptivity approach is implemented in a numerical framework based on the Discontinuous Galerkin (DG) method, that was already presented and validated in [41], which allows to extend seamlessly the LES concept to unstructured meshes. DG methods combine the high order of accuracy and low dissipation/dispersion properties with good parallel performances, since most of the computations are local to the element and only inter-element boundary fluxes must be communicated. The adaptation technique we employ is a $p-$adaptive approach, in which the polynomial degree is varied locally, rather than the mesh size, as in more standard $h-$adaptive methods. DG methods provide an interesting environment for $p-$adaptivity, since they do not require to enforce continuity constraints at the interelement boundaries. Furthermore, $p-$adaptive techniques are appealing since they allow to correct possible shortcomings of the computational mesh, as well as to perform dynamically adaptive simulations without extensive remeshing. Degree adaptation has been studied in the DG context in a great number of papers, see e.g. [18, 37, 42, 35, 24, 43]. For statistically steady state configurations, statically $p-$adaptive LES was shown in [13, 40, 44, 38] to lead to significant efficiency gains, while an example of dynamical $p-$adaptation is described in [36] in an ILES context.

In this paper, we will show how the adaptive method of [13, 40] can be applied locally and dynamically in time, in order to simulate efficiently and accurately transient phenomena. The proposed adaptive approach is presented in the framework of an otherwise rather conventional modal DG formulation, but could be extended also to other, more novel approaches. Given the difficulty in disentangling the effects of subgrid scale models from those of numerical diffusion, it should be stressed that an effective application of the proposed adaptive

method relies on the implicit assumption that the maximum polynomial degree achievable on a given mesh in these adaptive simulations is sufficient for the accurate resolution of the main turbulent structures of the flow on the same mesh. We have carried out a number of time dependent numerical simulations in two different configurations, namely, a temporally evolving mixing layer and the interaction of a vortex impinging on a square cylinder with the cylinder wake. The results obtained show that a significant reduction of the computational cost of LES can be achieved, reducing the number of degrees of freedom employed down to $30-40\%$ of those required by constant maximum polynomial degree simulations, while maintaining most quantitative indicators within less than 10% of those obtained in the corresponding constant maximum polynomial degree simulations. Furthermore, the results obtained show that the higher is the maximum polynomial degree allowed, the closer are the results of the adaptive method to the reference solutions, while the relative computational cost of the adaptive simulations decreases as the maximum polynomial degree allowed increases.

In Section 2, the model equations and numerical method are reviewed. In Section 3, the dynamical adaptivity approach is outlined. In Sections 4, 5, results of the numerical simulations on two significant test cases are presented. Finally, in Section 6 some conclusions are drawn and some perspectives of future development of this approach are discussed.

2. Model equations and numerical method

In this Section, the model equations and the numerical method will be briefly presented. For a more detailed description, we refer to [41], where this methodology was first introduced and validated for LES applications. The LES filtered Navier–Stokes equations for compressible flows can be written in dimensionless form as:

$$\partial_t \mathbf{U} + \nabla \cdot \mathbf{F} = 0 \tag{1}$$

where $\mathbf{U} = [\overline{\rho}, \overline{\rho}\widetilde{\mathbf{u}}^T, \overline{\rho}\widetilde{e}]^T$ are the prognostic resolved variables and $\mathbf{F} = \mathbf{F}^{\mathrm{a}} - \mathbf{F}^{\mathrm{v}} + \mathbf{F}^{\mathrm{sgs}}$ are the fluxes, composed by the advective fluxes

$$\mathbf{F}^{\mathrm{a}}(\mathbf{U}) = \begin{bmatrix} \overline{\rho}\widetilde{\mathbf{u}} \\ \overline{\rho}\widetilde{\mathbf{u}} \otimes \widetilde{\mathbf{u}} + \frac{1}{\gamma Ma^2}\overline{p}\mathcal{I} \\ \overline{\rho}\widetilde{h}\widetilde{\mathbf{u}} \end{bmatrix}, \tag{2}$$

the viscous fluxes

$$\mathbf{F}^{\mathrm{v}}(\mathbf{U}, \nabla\mathbf{U}) = \begin{bmatrix} 0 \\ \frac{1}{Re}\widetilde{\sigma} \\ \frac{\gamma Ma^2}{Re}\widetilde{\mathbf{u}}^T\widetilde{\sigma} - \frac{1}{\kappa RePr}\widetilde{\mathbf{q}} \end{bmatrix} \tag{3}$$

and finally the subgrid fluxes

$$\mathbf{F}^{\mathrm{sgs}}(\mathbf{U}, \nabla\mathbf{U}) = \begin{bmatrix} 0 \\ \tau \\ \frac{1}{\kappa}\mathbf{Q}^{\mathrm{sgs}} + \frac{\gamma Ma^2}{2}\left(\mathbf{J}^{\mathrm{sgs}} - \tau_{kk}\widetilde{\mathbf{u}}\right) \end{bmatrix}. \tag{4}$$

Here, $\bar{\cdot}$ and $\widetilde{\cdot}$ represent the grid filter and the Favre filter operators, so that $\overline{p}$ denotes the filtered pressure, $\overline{\rho}\widetilde{h} = \overline{\rho}\widetilde{e} + \overline{p}$ the resolved enthalpy and $\widetilde{\sigma}$ and $\widetilde{\mathbf{q}}$ the momentum and heat diffusive fluxes, respectively. Equations (1) are completed by the dimensionless state equation for a perfect gas

$$\overline{p} = \overline{\rho}\widetilde{T}, \tag{5}$$

where $\widetilde{T}$ is the filtered temperature. To close the system the constitutive equations must also be specified:

$$\widetilde{\sigma_{ij}} = \mu\widetilde{\mathcal{S}_{ij}}^{d}, \qquad \widetilde{q_i} = -\mu\partial_i\widetilde{T}, \tag{6}$$

where the rate of resolved strain tensor is defined as

$$\widetilde{\mathcal{S}_{ij}} = \partial_j\widetilde{u}_i + \partial_i\widetilde{u}_j \qquad \widetilde{\mathcal{S}_{ij}}^{d} = \widetilde{\mathcal{S}_{ij}} - \frac{1}{3}\widetilde{\mathcal{S}_{kk}}\delta_{ij} \tag{7}$$

and the dynamic viscosity, according to a power law, is

$$\mu(\widetilde{T}) = \widetilde{T}^{\alpha}. \tag{8}$$

with $\alpha = 0.7$. In the Local Discontinuous Galerkin approach [45], the equations are rewritten as a first order system

$$\begin{aligned} \partial_t \mathbf{U} + \nabla \cdot \mathbf{F}^{\mathrm{a}}(\mathbf{U}) &= \nabla \cdot \mathbf{F}^{\mathrm{v}}(\mathbf{U}, \boldsymbol{\mathcal{G}}) - \nabla \cdot \mathbf{F}^{\mathrm{sgs}}(\mathbf{U}, \boldsymbol{\mathcal{G}}), \quad (9) \\ \boldsymbol{\mathcal{G}} - \nabla \boldsymbol{\varphi} &= 0, \quad (10) \end{aligned}$$

where $\boldsymbol{\varphi} = [\widetilde{\mathbf{u}}^T, \widetilde{T}]^T$, so as to handle the viscous terms more conveniently in a DG setting. A tessellation $\mathcal{T}_h$ composed of non overlapping tetrahedral elements is defined in the domain Ω over which a discontinuous finite element space $\mathcal{V}_h$ is defined in the following way

$$\mathcal{V}_h = \{v_h \in L^2(\Omega) : v_h|_K \in \mathbb{P}^{p_K}(K), \forall K \in \mathcal{T}_h\}, \quad (11)$$

where $\mathbb{P}^{p_K}(K)$ denotes the space of polynomial functions of total degree p_K over the element K. The weak discrete form of equation (9) is derived using test functions belonging to the same space as the numerical solution. A modal DG approach is here applied, by using a hierarchical orthonormal polynomial basis for each element K in the finite dimensional space $\mathcal{V}_h$. Notice that this orthonormal basis is built on a reference element and then mapped back to the physical space, see the more detailed presentation e.g. in [21],[22]. The numerical approximation of the generic variable a it then expressed as

$$a_h|_K = \sum_{l=0}^{n_\phi(K)} a^{(l)} \phi_l^K, \quad (12)$$

where ϕ_l^K are the basis functions on element K, $a^{(l)}$ are the modal coefficients associated with the basis functions with corresponding index and

$$n_\phi(K) + 1 = |\mathbb{P}^{p_K}(K)|$$

is the number of basis functions required to span the polynomial space $\mathbb{P}^{p_K}(K)$ of degree p_K, defined in $\mathbb{R}^3$ as:

$$n_\phi(K) + 1 = \frac{1}{6}(p_K + 1)(p_K + 2)(p_K + 3) \quad (13)$$

To compute the advective flux $\{\mathbf{F}\}^{\mathrm{a}}$ the Rusanov flux [46] is employed, while a centred flux is used for the diffusive fluxes $\{\mathbf{F}\}^{\mathrm{v}}$, $\{\mathbf{F}\}^{\mathrm{sgs}}$ and for the gradient

variables flux $\{\boldsymbol{\varphi}\}$. It is important to remark that the previously outlined DG approach is rather conventional and not necessarily the best possible one. For example, the choice of the Rusanov flux is know to be suboptimal in some regimes, see the empirical findings in [47] and the analysis based on spatial eigensolution proposed in [11], [12]. Furthermore, aliasing is known to occur for the Euler equations, due to the rational form of the nonlinear fluxes, and de-aliasing techniques such as overintegration must be employed to guarantee stable simulations [48], [49], [50], unless specific entropy stable DG schemes are employed, see e.g. [51], [52]. For convenience, we only consider $p-$adaptivity in the present simpler framework, leaving its application in the context of more advanced DG methods to future work. After space discretization, equations (1) are advanced in time with an explicit, five-stages fourth-order strong stability preserving Runge-Kutta method proposed in [53].

In the present framework, as explained in detail in [41], the filtering operators are built in the DG spatial discretization. More specifically, along the lines proposed e.g. in [54, 55, 56], we define the filter operators in terms of approximate L^2 projectors. Given a subspace $\mathcal{V} \subset L^2(\Omega)$, let $\Pi_{\mathcal{V}} : L^2(\Omega) \to \mathcal{V}$ be the associated projector defined by

$$\int_\Omega \Pi_{\mathcal{V}} a \, v \, d\mathbf{x} = \int_\Omega a \, v \, d\mathbf{x}, \qquad \forall a, v \in \mathcal{V},$$

where the integrals are evaluated with appropriate quadrature rules. For $a \in L^2(\Omega)$, the filter $\bar{\cdot}$ is now defined by

$$\overline{a} = \Pi_{\mathcal{V}_h} a, \tag{14}$$

or equivalently $\overline{a} \in \mathcal{V}_h$ such that

$$\int_K \overline{a} v_h \, d\mathbf{x} = \int_K a v_h \, d\mathbf{x} \qquad \forall K \in \mathcal{T}_h, \quad \forall v_h \in \mathcal{V}_h. \tag{15}$$

Notice that the application of this filter is built in the discretization process and equivalent to it. The LES filtering $\bar{\cdot}$ is thus equivalent to the projection onto the employed finite dimensional solution subspace, while the Favre filter operator $\tilde{\cdot}$ is defined as

$$\widetilde{a} = \frac{\overline{\rho a}}{\overline{\rho}}. \tag{16}$$

In the simulations presented in this paper, two different subgrid models have been employed, the classical Smagorinsky model and an anisotropic dynamic model, whose description is summarized in the next two subsections.

2.1. Eddy viscosity model

The compressible extension of the classical Smagorinsky model [41] has been applied to the simulations of the flow around a square section cylinder presented in Section 5. In this model, the anisotropic part of the subgrid stresses is modelled by a scalar eddy viscosity $\nu^{sgs} = C_S^2 \Delta^2 |\widetilde{\mathcal{S}}| f_D$, so as to obtain

$$\tau_{ij} - \frac{1}{3}\tau_{kk}\delta_{ij} = \overline{\rho}\nu^{sgs}\mathcal{S}^d_{ij} \tag{17}$$

where $C_S = 0.1$ is the Smagorinsky constant, $|\widetilde{\mathcal{S}}| = \sqrt{\widetilde{\mathcal{S}_{ij}}\widetilde{\mathcal{S}_{ij}}}$ and

$$f_D = 1 - \exp(y^+/25)$$

is the Van Driest damping, which is a function of the distance from the wall y^+ in wall units. In the model, the filter width is determined elementwise as

$$\Delta(K) = \sqrt[3]{\frac{Vol(K)}{n_\phi(K)+1}}. \tag{18}$$

Following [57, 58], the subgrid heat and kinetic energy fluxes are modelled as

$$Q_i = -\overline{\rho}\nu^{sgs}\Delta^2|\widetilde{\mathcal{S}}|\partial_i\widetilde{T}, \qquad J_i = -2\widetilde{u}_k\tau_{ik} + \widetilde{u}_i\tau_{kk}. \tag{19}$$

2.2. Anisotropic dynamic model

The anisotropic model proposed in [59] and extended to compressible flows in [41] has been used in the mixing layer simulations presented in Section 4. In this model, the subgrid stress tensor is assumed to be proportional to the strain rate tensor through a fourth order symmetric tensor

$$\tau_{ij} = -\overline{\rho}\Delta^2|\widetilde{\mathcal{S}}|\mathcal{B}_{ijrs}\widetilde{\mathcal{S}}_{rs}. \tag{20}$$

Thanks to a rotation tensor a_{ij}, the tensor $\mathcal{B}_{ijrs}$ can be contracted into a second order symmetric tensor $\mathcal{C}_{\alpha\beta}$:

$$\mathcal{B}_{ijrs} = \sum_{\alpha,\beta=1}^{3} \mathcal{C}_{\alpha\beta}a_{i\alpha}a_{j\beta}a_{r\alpha}a_{s\beta}. \tag{21}$$

In particular, assuming a_{ij} equal to the components of the orthogonal Cartesian reference frame basis, one obtains

$$\tau_{ij} = -\overline{\rho}\Delta^2\mathcal{C}_{ij}|\widetilde{\mathcal{S}}|\widetilde{\mathcal{S}}_{ij}. \tag{22}$$

The dynamic computation of the components $\mathcal{C}_{\alpha\beta}$ relies on the introduction of a test filter operator $\widehat{\cdot}$ defined for $v \in L^2(\Omega)$ as $\widehat{v} = \Pi_{\widehat{\mathcal{V}}_h} v$, where $0 \leq \widehat{p}_K < p_K$ and

$$\widehat{\mathcal{V}}_h = \{v_h \in L^2(\Omega) : v_h|_K \in \mathbb{P}^{\widehat{p}_K}(K),\, \forall K \in \mathcal{T}_h\}, \tag{23}$$

The application of the dynamic procedure, as described in detail in [60], provides the expression for the products $(\Delta^2\mathcal{C}_{ij})$, which are then averaged over each element. Clipping is then applied to ensure positive total dissipation.

Similarly, the anisotropic dynamic procedure is also applied to model the subgrid heat flux

$$Q_i = -\overline{\rho}(\Delta^2\mathcal{C}_j^Q)|\widetilde{\mathcal{S}}|\partial_j\widetilde{T}, \tag{24}$$

and the subgrid kinetic energy flux

$$J_i = -\overline{\rho}(\Delta^2\mathcal{C}_j^J)|\widetilde{\mathcal{S}}|\partial_j\left(\frac{1}{2}\widetilde{u}_k\widetilde{u}_k\right). \tag{25}$$

3. A dynamically $p-$adaptive approach

A physically based refinement indicator especially suited for LES has been proposed by the authors in [13, 40]. This indicator is based on the classical structure function

$$D_{ij} = \langle [u_i(\boldsymbol{x}+\boldsymbol{r},t) - u_i(\boldsymbol{x},t)]\,[u_j(\boldsymbol{x}+\boldsymbol{r},t) - u_j(\boldsymbol{x},t)]\rangle\,, \tag{26}$$

where $\langle\cdot\rangle$ represents the expected value operator. The structure function has been widely used to study turbulence statistics and it is known to be directly related to the subgrid stresses [61, 62, 63]. Larger values of the structure function computed inside the element denote a poorly correlated velocity field and the need for higher resolution, while lower values denote a highly correlated velocity field, which implies a well resolved turbulent region or laminar conditions, hence

the possibility to employ lower resolution. The degree adaptation indicator is then defined as:

$$Ind_{SF}(K) = \sqrt{Q(K)} = \sqrt{\sum_{ij} \left[D_{ij}(K) - D_{ij}(K)^{iso}\right]^2} \tag{27}$$

where D_{ij}^{iso} is the structure function in isotropic conditions [64], which is defined as

$$D_{ij}^{iso}(\boldsymbol{r}, t) = D_{NN}(r, t)\delta_{ij} + \left(D_{LL}(r, t) - D_{NN}(r, t)\right) \frac{r_i r_j}{r^2} \tag{28}$$

where $r = \|\boldsymbol{r}\|$ and D_{LL}, D_{NN} are the longitudinal and transverse structure functions, respectively. More specifically, the indicator is computed by the following procedure:

1. choose a pair of points defining $\boldsymbol{x}$ and $\boldsymbol{r}$ in K
2. compute the structure function $D_{ij}(K)$ based on $\boldsymbol{x}$, $\boldsymbol{r}$ and the simulated velocity field
3. compute D_{NN} and D_{LL} by a least square fit of (28) to the structure function values within the element
4. compute the indicator 27.

In order to reduce the arbitrariness in the choice of $\boldsymbol{x}$ and $\boldsymbol{r}$ for the computation of (26), its value is computed for each couple of element vertices and then averaged.

In [13], this procedure was shown to be effective in a static, locally $p-$adaptive framework, producing accurate results with a significant reduction in computational cost. However, static adaptivity presents some limitations, since the resolution is fixed at the beginning of the simulation and constant in time. In the simulation of a transient phenomenon, for which a time resolved solution is sought rather than a statistical average, employing a dynamic adaptivity framework is necessary. In our implementation of dynamic degree adaptation, the indicator (27) is computed at runtime at time intervals Δt_i and averaged over time. Once the indicator has been averaged on a time interval Δt_a which is sufficiently larger than Δt_i, but still small with respect to the time scale

of the motion of the main turbulent structures, a new polynomial distribution is computed based on the indicator values and the flow field approximation is updated, by either reducing or increasing the number of degrees of freedom employed in each element. Notice that, with the above procedure, the quality of the results may depend on the chosen length Δt_a averaging parameter. This dependency has not been investigated so far. A possible alternative is to avoid the time averaging of the indicator and to update the polynomial degrees at all time steps, as it was done for the inviscid simulations presented in [21], [22]. This may however result in a larger computational cost.

In this work, the admissible polynomial degrees ranged from 2 to 5. Three indicator thresholds $\epsilon_1 < \epsilon_2 < \epsilon_3$ were employed. Elements with a value of the indicator (27) lower than $\epsilon_1$were assigned the lowest allowed polynomial degree 2, those with values between ϵ_1 and ϵ_2 were assigned the polynomial degree 3, those with values between ϵ_2 and ϵ_3 were assigned the polynomial degree 4 and those with values above ϵ_3 were assigned the value 5. Polynomial degrees were only allowed to increase or decrease by one degree in each adaptation. Since the solution is represented by a hierarchical basis, when lowering the polynomial degree, the contribution associated to the removed modes is simply discarded, while when raising the polynomial degree the coefficients of the newly added modes are initialized to zero, to be updated by the subsequent time evolution.

Clearly, the choice of the threshold parameters is a critical step in this as in any other adaptive algorithm. In principle, their choice should be aimed at maintaining the maximum possible accuracy given some estimate of the available computational resources. Ideally, very high maximum polynomial degrees would be allowed and a large number of thresholds would be used. The search for an optimal threshold choice is still an open issue and will be the focus of future work. Here, as well as in our previous paper [13] on static adaptation, the choice was performed by computing the indicator on the flow fields of lower resolution simulations. Specifically, simulations with constant degree $p = 2$ were used for the tests reported in Sections 4 and 5. The values of the thresholds were then adjusted for each case so as to obtain for the initial datum a number of

degrees of freedom (dofs) corresponding approximately to a fraction of that of the analogous constant degree $p = 3$ simulation. It is to be remarked that this choice is only motivated by the goal of performing a fair efficiency assessment and should not be regarded as optimal. Notice also that no constraint has been imposed on the spatial distribution of the local polynomial degrees. As a consequence, the polynomial degrees of neighbouring elements could differ in principle by more than unity. On the other hand, this seems to occur in practice only at a very limited number of locations, as it can be seen from the results presented in Sections 4 and 5. The possible sensitivity of the results to these abrupt variations still has to be investigated in depth, but so far no evidence of inaccuracies or instabilities related to this fact has been found. Furthermore, restrictions to enforce a smoother spatial variation of the polynomial degree could be easily enforced if necessary.

Finally, it should be remarked that the procedure outlined above can lead to unbalances between the computational load of different processors in a parallel run. The implementation of a full dynamic load balancing is beyond the scope of the present work, whose focus is mostly on the assessment of the accuracy of the proposed adaptive method. As a consequence, in all the numerical experiments presented below, the computational load among the processors is approximately balanced at the beginning of the simulation only, which is clearly suboptimal with respect to full parallel efficiency. Indeed, the results will not in general be assessed based of the CPU time required, but rather on the total number of the degrees of freedom employed in the adaptive versus non adaptive simulations. On the other hand, it must be noted that, even in this suboptimal configuration, the adaptive simulation always led to a net reduction in computational cost with respect to their fixed degree counterparts. In order to assess the effective reduction in the CPU time required, further work on code optimization is needed, along with the development and application of load balancing approaches such as those employed e.g. in [36, 65].

4. Temporally evolving mixing layer

In a first assessment of the adaptive LES approach outlined in the previous sections, an isothermal time developing mixing layer was simulated. The temporal mixing layer represents an interesting test case for LES, due to its simplicity and advantages from the computational viewpoint, as well as the complexity of the physics related to the mixing, see e.g. the discussions in [66, 67, 68, 69]. The commonly employed configuration to represent a mixing layer flow was employed, imposing periodic boundary conditions on the mean flow and in the spanwise directions. Thanks to the periodicity in the streamwise direction, uncertainties related to the imposition of inlet and outlet boundary conditions are avoided. In the simulations presented here, the anisotropic dynamic subgrid model [41, 59] has been used, in which the filter width is included in the coefficients to be dynamically determined. A further application of this approach is presented in [60]. For the simulations with maximum degree $p = 5$, the value $\widehat{p}_K = 3$ was used, while for the simulations with maximum degree $p = 3, 4$ the value $\widehat{p}_K = 2$ was used instead.

A sketch of the flow configuration is shown in Figure 1. The mixing layer is characterized by two parallel flows with different velocities U_1 and U_2. The convection velocity of the isothermal mixing layer, defined as $U_c = (U_1 + U_2)/2$, is the velocity that transports the vortical structures at the centreline. In the configuration we considered, the convection velocity is assumed to be zero, so that the eddies do not travel inside the domain by means of the flow, but only move by mutual interaction. As a consequence, $U_1 = -U_2$ and $|U_1| = |U_2| = (U_1 - U_2)/2$. The reference frame is chosen so that the x axis is aligned with the main direction of the flow centered at the middle of the domain, while the y and z axis denote transverse and lateral directions, respectively. The initial vorticity thickness, defined as

$$\delta_{\omega r} = \frac{U_1 - U_2}{\max(dU/dy)}$$

is chosen as reference length for the non-dimensionalization. The initial velocity jump $\Delta U_r = (U_1 - U_2)$ is used as reference velocity, the initial uniform density ρ_r

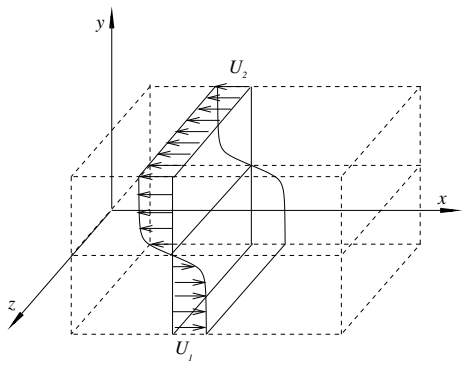

Figure 1: Sketch of the mixing layer configuration.

and temperature T_r are used as reference density and temperature, respectively. The fundamental dimensionless groups are then

$$Re = \frac{\rho_r \Delta U_r \delta_{\omega r}}{\mu_r} = 400, \quad Pr = \frac{\mu_r c_p}{k} = 0.71, \quad Ma = \frac{\Delta U_r}{\sqrt{\gamma R T_r}} = 0.2.$$

Notice that it is also customary (see e.g. [66]) to consider also the convective Mach number, which in the present isothermal configuration amounts to $Ma_c = Ma/2$. The temporally evolving mixing layer develops from a specified initial condition. In these computations, we use a hyperbolic tangent as the base velocity profile for the longitudinal component

$$U(y) = \frac{U_1 + U_2}{2} + \frac{U_1 - U_2}{2} \tanh(2y) \tag{29}$$

where $U_1 = 0.5$ and $U_2 = -0.5$ so that $U_c = 0$. A similar configuration was considered in [66, 70, 71], where however the focus was mostly on acoustic effects. Similarly to [70, 71], a 3D incompressible disturbance is added to the base velocity profile to initiate the transition process. It consists of harmonic

disturbances expressed as

$$
\begin{aligned}
u' &= Ae^{-\sigma y^2}\frac{\sigma}{\pi}L_x y\left[\sin\left(\frac{16\pi}{L_x}x\right)+\frac{1}{8}\sin\left(\frac{8\pi}{L_x}x\right)+\frac{1}{16}\sin\left(\frac{4\pi}{L_x}x\right)\right]\\
v' &= Ae^{-\sigma y^2}\left[\cos\left(\frac{16\pi}{L_x}x\right)+\frac{1}{8}\cos\left(\frac{8\pi}{L_x}x\right)+\frac{1}{16}\cos\left(\frac{4\pi}{L_x}x\right)\right]\\
w' &= Ae^{-\sigma y^2}\frac{\sigma}{\pi}L_x y\left[\sin\left(\frac{16\pi}{L_x}x\right)+\frac{1}{8}\sin\left(\frac{8\pi}{L_x}x\right)+\frac{1}{16}\sin\left(\frac{4\pi}{L_x}x\right)\right]\\
&\quad\left[\cos\left(\frac{16\pi}{L_x}x\right)+\frac{1}{8}\cos\left(\frac{8\pi}{L_x}x\right)+\frac{1}{16}\cos\left(\frac{4\pi}{L_x}x\right)\right]
\end{aligned}
$$

where $A = 0.025(U_1 - U_2)$ and the decay in y-direction is governed by $\sigma = 0.05$. Moreover, a 3D white noise perturbation is added to the initial velocity field, generated for each mesh node by a logistic map rescaled to take values on $[-A, A]$ and multiplied by the attenuation factor $e^{-\sigma y^2}$, see [41] for a more detailed description. Uniform pressure $p = 1$ and density $\rho = 1$ are used to initialize the simulation. The longitudinal dimension of the computational domain must be large enough to allow at least for the merging of two principal vortical structure, so it must be taken as a multiple of the wavelength λ_a characterizing the most unstable perturbation, which according to the analysis in [67] is given in this context by $\lambda_a = 7.66$. In the present simulation, the size in the streamwise direction has been chosen $L_x = 8 \times \lambda_a = 60.8$, so that up to three vortices are allowed to merge. In the normal direction, the computational domain extends for $-30 \leq y \leq 30$, while in spanwise direction $L_z = 30.4$. Periodic boundary conditions are applied in the statistically homogeneous x and z directions, while a sponge layer is employed at the top and bottom boundaries, so that the effective size of the computational domain in the y direction is equal to 80.

The computational mesh is built first subdividing the domain in $N_{hx} \times N_{hy} \times N_{hz} = 20 \times 36 \times 10$ hexahedra. Each hexahedron is then split into 6 tetrahedra, yielding a total of 43200 tetrahedral elements. The actual resolution depends on the local polynomial order. In the case of constant local degree, the spacing in each direction can be computed as $\Delta_i = L_i/[N_{hi}(6n_\phi + 1)^{\frac{3}{2}}]$, while the average resulting values for each value of p employed are displayed in Table 1. Notice that the simulations with $p = 5$ were repeated on a mesh with

$6 \times 28 \times 48 \times 14 = 112,896$ tetrahedral elements, thus increasing the number of elements by almost 50% in each direction. In this test case, overintegration was employed as de-aliasing technique in the numerical computation of the integrals appearing in the formulae of Section 2. More specifically, three more quadrature nodes were used in each dimension than the minimum number required by approximation theory.

A preliminary study of the mixing layer in the present configuration was presented in [72], where the sensitivity of the results to the choice of spatial resolution and subgrid scale model was checked. The objective of the present work is to test the $p-$adaptivity technique in a time evolving flow. For this purpose, the results obtained with polynomial degree dynamically adapting in space and time are compared with the results obtained with constant fourth and third degree polynomials.

To set the values of the adaptation thresholds, as discussed in Section 3, the structure function indicator was evaluated on the velocity field obtained with constant $p = 2$ at the final dimensionless time $t = 150$. Thresholds were then chosen in order to obtain, for that field, an adapted number of degrees of freedom (dofs) lower than 80% of the corresponding number of dofs in the constant $p = 3$ case. The resulting threshold values are then $\epsilon_1 = 10^{-6}$, $\epsilon_2 = 10^{-3}$, $\epsilon_3 = 5 \times 10^{-3}$. The dynamical $p-$adaptation was carried out by computing the indicator value at intervals $\Delta t_i = 0.0375$ and averaging them over intervals $\Delta t_a = 0.075$, while the value $\Delta t = 0.0075$ was used for time integration.

All the simulations were carried out on the Marconi cluster at CINECA, using 272 KNL processors. In Figure 2, the total number of dofs for the adaptive simulations divided by the values for the corresponding constant polynomial degrees (reported in Table 1) are shown as a function of time. The reduction of the number of dofs using $p-$adaptivity is evident, since the adaptive simulation requires less than 50% of the dofs for the $p = 4$ case and less than 30% of the dofs for the $p = 5$ case. The spatial resolution achieved in each simulation is detailed in Table 1, while the core hours necessary to perform the simulations are reported in Table 2. In spite of the absence of a specific dynamic load

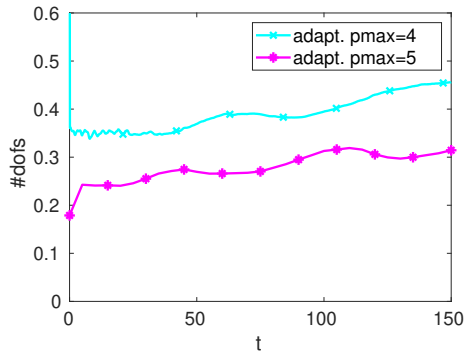

Figure 2: Total number of degrees of freedom during the dynamic adaptive simulations of mixing layer simulation, normalised by the number of degrees of freedom for the homogeneous distribution of the corresponding maximum degree.

	$N_{hx} \times N_{hy} \times N_{hz}$	Δ_x	Δ_y	Δ_z
$p = 5$ high res.	$28 \times 48 \times 14$	0.31	0.18	0.31
$p = 5$	$20 \times 36 \times 10$	0.44	0.24	0.44
$p = 4$	$20 \times 36 \times 10$	0.51	0.28	0.51
$p = 3$	$20 \times 36 \times 10$	0.61	0.34	0.61
$p-$adaptive $p_{max} = 4$	$20 \times 36 \times 10$	0.51–0.77	0.28–0.42	0.51–0.77
$p-$adaptive $p_{max} = 5$	$20 \times 36 \times 10$	0.44–0.77	0.24–0.4	0.44–0.77

Table 1: Spatial resolution employed for the mixing layer simulations using uniform polynomial degree distribution $p = 5$, $p = 4$, $p = 3$ and $p-$adaptive distribution with maximum polynomial degrees 4 and 5, respectively.

balancing procedure, the $p-$adaptive technique also yields a reduction of the required CPU time, which has a value only marginally larger than that of the $p = 3$ simulation for the adaptive $p_{max} = 4$ one and only marginally larger than that of the $p = 4$ simulation for the adaptive $p_{max} = 5$ case, which required 65% the CPU time of the constant $p = 5$ degree simulation. On the other hand, the sub-optimal nature of the present implementation is highlighted by the fact that the adaptive $p_{max} = 4$ simulation required more CPU time than the $p = 3$ case, even though it involved less dofs.

The polynomial degree distribution, the density and the streamwise compo-

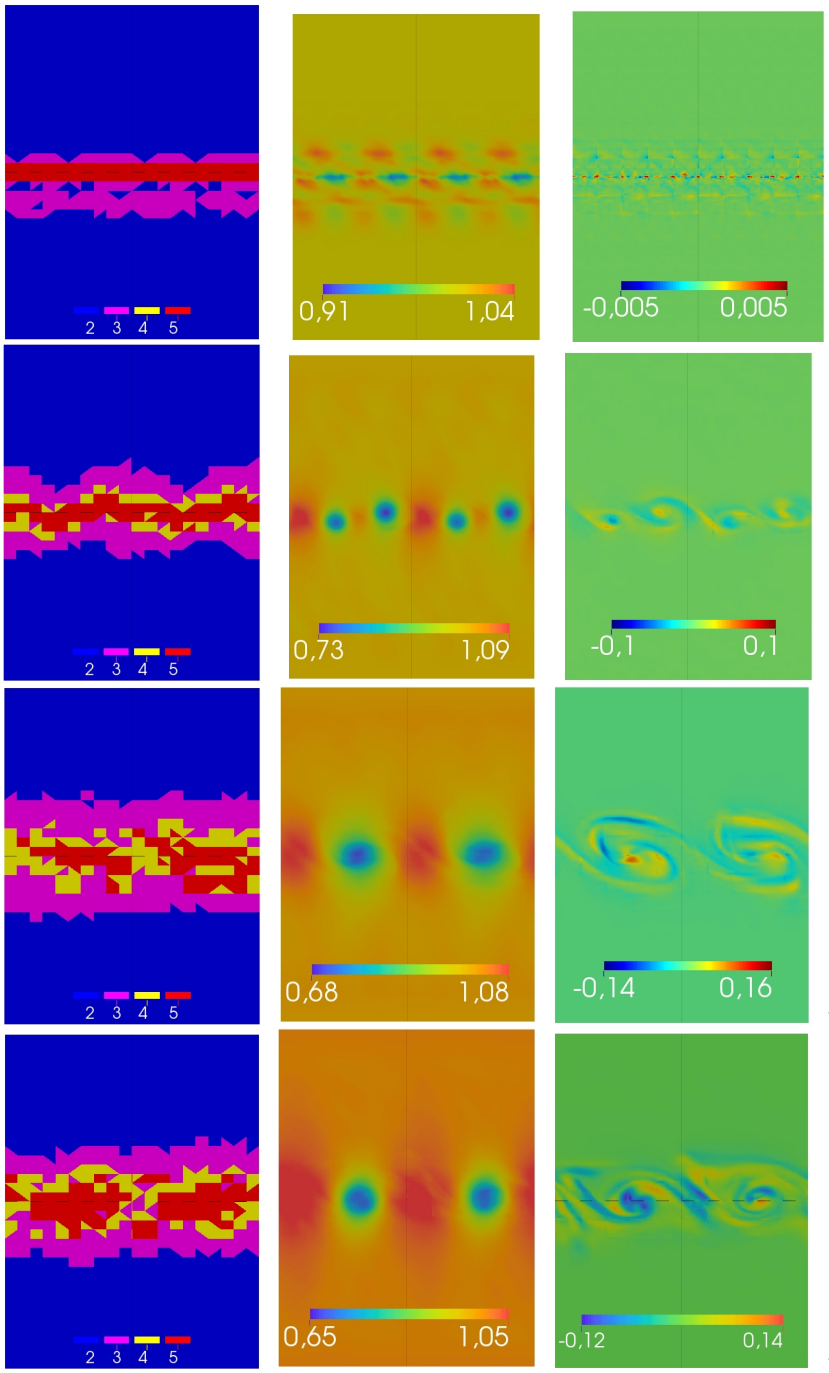

Figure 3: Results of the $p-$adaptive simulation, with maximum degree $p = 5$, of the temporal mixing layer plotted in the plane $z = 0$ at times $t = 4, 60, 105, 150$: polynomial degree distribution (left); density (centre); spanwise velocity component (right).

	Number of dofs	Core hours
$p = 5$ high res.	6.3×10^6	53400
$p = 5$	2.42×10^6	20100
$p = 4$	1.51×10^6	12600
$p = 3$	8.64×10^5	9000
$p-$adaptive $p_{max} = 4$	6.1×10^5 (average)	9300
$p-$adaptive $p_{max} = 5$	6.7×10^5 (average)	13200

Table 2: Number of degrees of freedom and core hours required for the mixing layer simulations using uniform polynomial degree distribution $p = 5$, $p = 4$, $p = 3$ and $p-$adaptive with maximum polynomial degree 4 and 5, respectively.

nent of the velocity, at different instants, in the plane $z = 0$, are represented in Figure 3. In the initial condition, the elements with highest degree $p = 5$ are concentrated along the middle of the domain, where high resolution is required. Then, the region with higher polynomial degree expands in space during time, adapting to the merging of the vortices, to the diffusion of the turbulent structures and to the growth of the layer thickness. An important quantity for the characterization of the mixing layer is the momentum thickness, defined as

$$\delta_\theta(t) = \int \overline{\rho}(\frac{1}{2} - \tilde{u})(\frac{1}{2} + \tilde{u})dy. \tag{30}$$

The time evolution of this quantity is represented in Figure 4. Notice that slope variations in its time evolution are associated to the merging of the vortices. This time evolution can be compared to some extent with that of Fig. 4 in [66], considering that, due to the different scaling, our time unit 150 corresponds approximately to the time unit 660 in [66]. Furthermore, in [66] the values of the Reynolds and Mach numbers are $Re = 750$ and $Ma_c = 0.3$, respectively while the values employed here are $Re = 400$ and $Ma_c = 0.1$. Even though full convergence is not achieved, it can be observed that each adaptive simulation reproduces well the corresponding fixed degree simulation. Furthermore, the values obtained for the constant degree $p = 3$ seem out of the range of the reference values in [66].

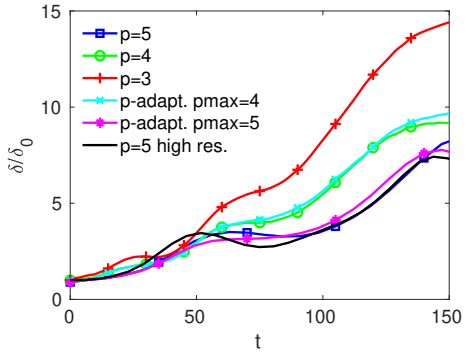

Figure 4: Growth of the momentum thickness, normalised by its initial value, in time, for the $p-$adaptive simulations and for uniform degree cases $p = 3$, $p = 4$, $p = 5$.

A similar behaviour can be observed in the spanwise and streamwise averaged density and velocity profiles shown in Figure 5, in the mean normal stress profiles shown in Figure 6 and in the turbulent kinetic energy profile shown in Figure 7(a). No clear convergence is achieved and, even at the finest resolution that could be employed, the flow may not be fully resolved. However, the adaptive simulations yield in general results that are close to those of the corresponding fixed degree simulation and that improve as the maximum allowed degree is increased.

In Figure 7(b), the subgrid scale (SGS) kinetic energy in the constant $p = 3$ case is clearly larger than in the other cases, due to the lower resolution that requires more intense contribution from the model. In the adaptive simulations, the SGS kinetic energy for the $p_{max} = 4$ case is closer to that of the $p = 3$ case, showing that at this resolution the adaptation procedure is probably unable to cope with the excess of numerical diffusion coming from the reduction in degree in some elements. On the other hand, for the $p_{max} = 5$ adaptive case a SGS kinetic energy profile much closer to that of the corresponding constant degree $p = 5$ is observed.

Concluding this analysis, we can affirm that the $p-$adaptive solutions display a behaviour quite similar to those obtained with the corresponding constant degree values, but e.g. for the $p = 5$ case they require about 30% of the number

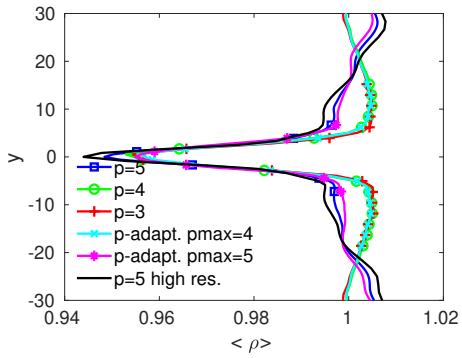

(a) $t = 60$

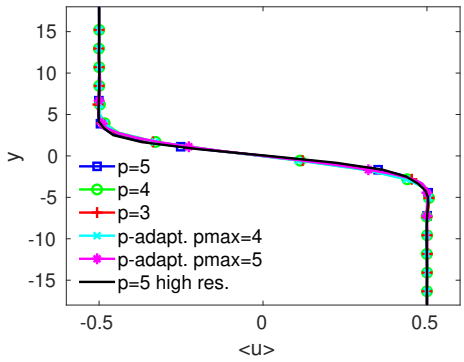

(b) $t = 60$

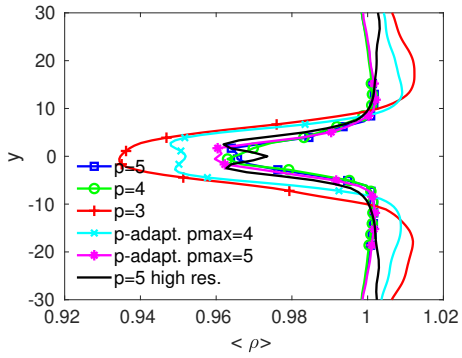

(c) $t = 105$

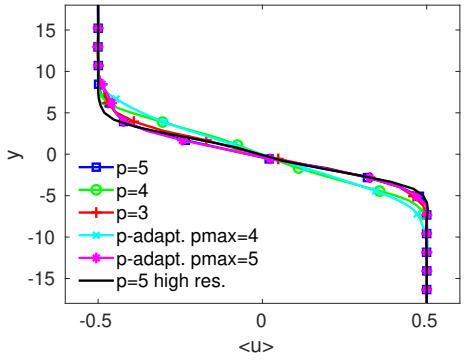

(d) $t = 105$

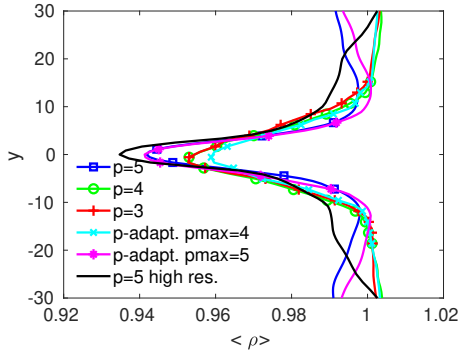

(e) $t = 150$

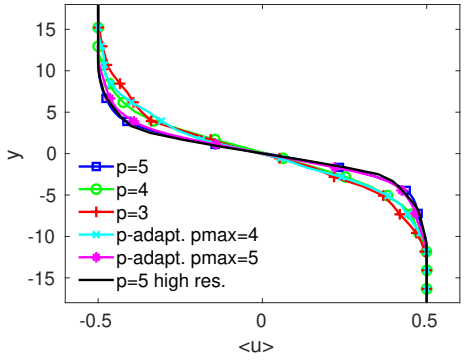

(f) $t = 150$

Figure 5: Mean profiles for density (left) and longitudinal velocity component (right) for the mixing layer at different times t.

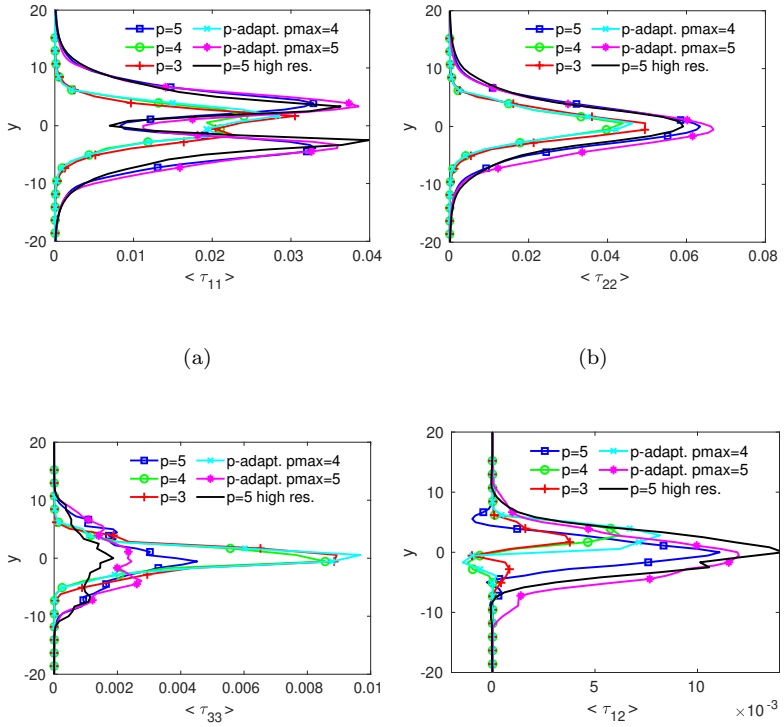

(a) (b)

(c) (d)

Figure 6: Mean profiles of the total turbulent stresses for the mixing layer at time $t = 150$.

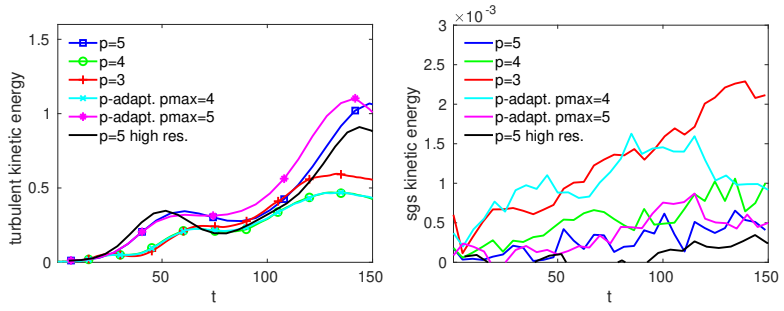

(a) (b)

Figure 7: Resolved turbulent kinetic energy (a) and SGS kinetic energy (b) in function of time for the mixing layer simulations.

of dofs and about 60% of CPU time for this test case, in spite of a sub-optimal implementation that did not employ any run-time load balancing. Moreover, the structure function indicator, which was proven successful in static adaptation in [13], is shown to be suitable also for simulation of transitional flows using a dynamic adaptation in time.

5. Interaction of Vortex and Square Section Cylinder

A body-vortex interaction flow represents another interesting time dependent problem to test dynamic $p-$adaptivity. Here, a vortex interacting with a square section cylinder at $Re = 22000$ and $Ma = 0.3$ is considered. The configuration we consider was employed e.g. in [73] and has been used to assess statically adaptive LES simulations of the standard flow around a square section cylinder in [13, 40, 74]. We refer to [13] for a more extensive literature review on this benchmark. In particular, experimental results on this configuration are reported in [75, 76, 77, 78], DNS simulations in [79] and LES results in [78, 80, 81, 82, 83]. The Smagorinsky SGS model described in Section 2.1 was applied for this test.

The results obtained with polynomial adaptivity are compared with the solution obtained with uniform in space and constant in time degree distribution. The solution computed with constant $p = 5$ is taken as reference, along with the results presented in the previously listed papers.

The computational domain employed is box shaped and a 2D sketch of the geometry is represented in Figure 8. Denoting the cylinder side with $H = 1$, which is used as reference length, the inflow length has been taken equal to $L_f = 10$, while the outflow length is equal to $L_r = 20$. The cylinder is vertically centered with a distance of $L_s = 10$ from the upper and lower boundaries. The domain is extruded in the spanwise direction by a length equal to $L_z = 4$.

Non-slip isothermal boundary conditions are imposed on the cylinder walls, while homogeneous Neumann boundary conditions are imposed on the upper and lower boundaries of the domain and periodic conditions are enforced in the

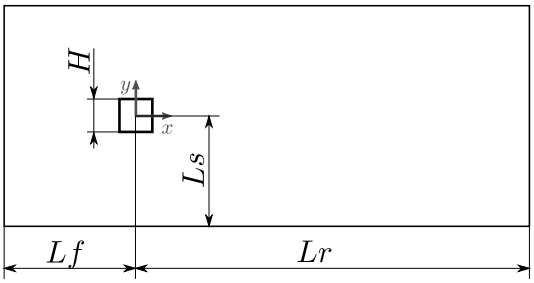

Figure 8: 2D sketch of the square section cylinder case geometry. The lines on which the statistics are calculated and plotted are highlighted.

spanwise direction to simulate an infinite span cylinder. Dirichlet conditions corresponding to the far field values are imposed at the inflow and outflow boundaries, with sponge layers to avoid reflections of disturbances from the boundaries. At the inflow, a uniform far-field velocity is imposed.

The mesh employed consists of 23816 tetrahedra arranged in an outer unstructured area and a structured O-grid mesh around the cylinder, which is then extruded in the spanwise direction. The effective resolutions around the cylinder for the different polynomial degrees employed are reported in Table 3. Notice that in this case no overintegration was necessary to achieve stable simulations.

In a first set of simulations, aimed at assessing the quality of the constant degree LES results, this configuration was computed on the above described mesh with constant polynomial degrees $p = 3, 4, 5$. Notice that this extends the results presented in [13], in which only the cases $p = 3, 4$ were considered. The results obtained are reported in Table 4 along with reference results presented in the literature for some common global quantitative parameters. Furthermore, the profiles of several relevant quantities are reported at three different locations in Figures 10-13. Notice that, only for these statistically steady state simulations, time averaging was performed over a period of 60 non dimensional time units. The results obtained are well in the range of other LES studies and a definite convergence pattern is observed for the Strouhal number. Furthermore,

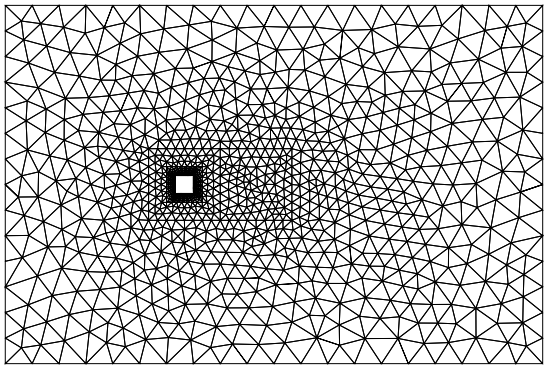

Figure 9: 2D section of the mesh employed for the flow around the square section cylinder

	Δ_n	Δ_t	Δ_z
$p = 5$	0.006	0.020	0.115
$p = 4$	0.008	0.024	0.135
$p = 3$	0.010	0.029	0.163
$p = 2$	0.012	0.036	0.205

Table 3: Resolution at the wall around the square section cylinder, for polynomial degree $p = 5$, $p = 4$, $p = 3$ and $p = 2$: Δ_n in normal to the wall direction, Δ_t in tangential direction, Δ_z in spanwise direction.

the profiles show that the $p = 5$ simulations are well resolved and generally in good agreement with the experimental data.

After the previous assessment of the constant degree simulation, a vortex is superimposed to an initial condition corresponding to a developed flow around the cylinder, obtained by a previous LES simulation, in order to simulate the cylinder-vortex interaction. The axis of the introduced vortex is parallel to the z direction. The vortex is defined by the velocity components

$$u = U_\infty - C_v \frac{y}{R_v^2} \exp\left(-\frac{x^2+y^2}{2R_v^2}\right), \tag{31}$$

$$v = C_v \frac{x}{R_v^2} \exp\left(-\frac{x^2+y^2}{2R_v^2}\right), \tag{32}$$

$$w = 0, \tag{33}$$

	St	$< C_d >$	rms(C'_d)	rms(C'_l)
experiments	0.13	2.1	0.18	1.2
DNS	0.132	2.18	0.205	1.71
LES	0.09–0.15	2.01–2.77	0.14–0.27	1.15–1.79
$p = 2$	0.1462	2.321	0.1480	1.204
$p = 3$	0.1487	2.352	0.1605	1.305
$p = 4$	0.141	2.398	0.1930	1.374
$p = 5$	0.136	2.4	0.1677	1.43

Table 4: Global results for the flow around the square section cylinder at $Re = 22000$ and $Ma = 0.3$. The results obtained with homogeneous polynomial degree $p = 2, 3, 4$ and 5 are compared with experimental data [76, 77, 78], with results from DNS [79] and LES [78, 80, 81, 82, 83].

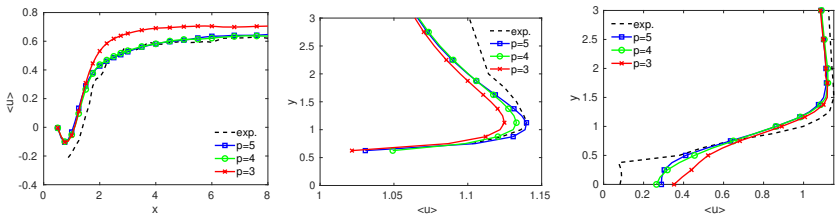

(a) (b) (c)

Figure 10: Streamwise component of the mean velocity profile in the flow around the square section cylinder: 10(a) along the $y = 0$ line in the wake, 10(b) along the $x = -0.5$ line on the corner, 10(c) along the $x = 2.5$ line in the wake. The solutions obtained with constant polynomial degrees $p = 3$, $p = 4$ and $p = 5$ are compared with experimental results in [75].

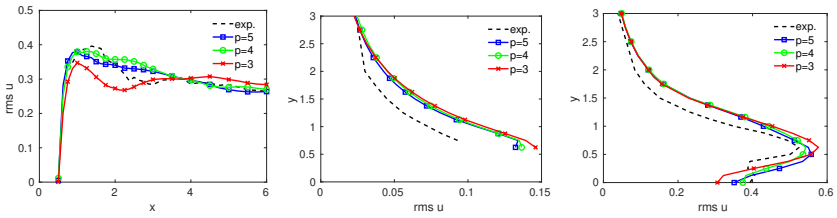

(a) (b) (c)

Figure 11: Square root of the total (resolved plus modelled) streamwise component of turbulent stresses in the flow around the square section cylinder: 11(a) along the $y = 0$ line in the wake, 11(b) along the $x = -0.5$ line on the corner, 11(c) along the $x = 2.5$ line in the wake. The solutions obtained with constant polynomial degrees $p = 3$, $p = 4$ and $p = 5$ are compared with experimental results in [75].

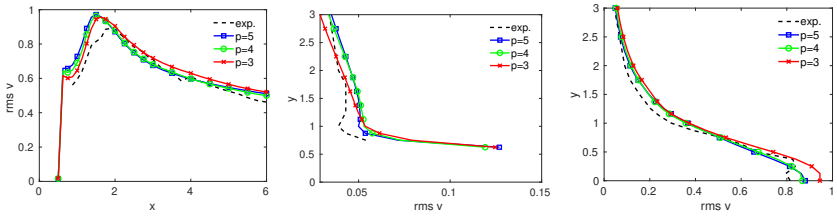

(a) (b) (c)

Figure 12: Square root of the total (resolved plus modelled) y component of turbulent stresses in the flow around the square section cylinder: 12(a) along the $y = 0$ line in the wake, 12(b) along the $x = -0.5$ line on the corner, 12(c) along the $x = 2.5$ line in the wake. The solutions obtained with constant polynomial degrees $p = 3$, $p = 4$ and $p = 5$ are compared with experimental results in [75].

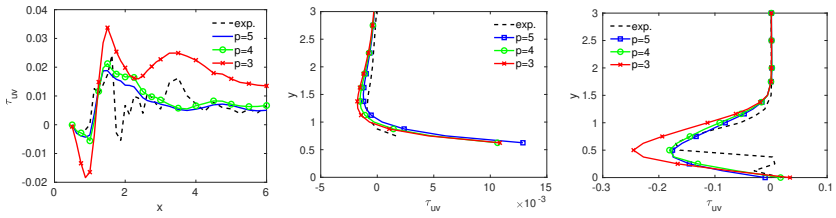

(a) (b) (c)

Figure 13: Total (resolved plus modelled) shear component of turbulent stresses in the flow around the square section cylinder: 13(a) along the $y = 0$ line in the wake, 13(b) along the $x = -0.5$ line on the corner, 13(c) along the $x = 2.5$ line in the wake. The solutions obtained with constant polynomial degrees $p = 3$, $p = 4$ and $p = 5$ are compared with experimental results in [75].

where C_v denotes the vortex strength, R_v is the vortex radius, $r^2 = x^2 + y^2$ is the distance in the $x-y$ plane from the vortex center and U_∞ is the uniform flow over which the vortex is superimposed [84]. The maximum tangential velocity is obtained at $r = R_v$ and is given by $v_{\theta_{max}} = \frac{C_v}{R_v} \exp(-\frac{1}{2})$. Regarding the other variables, it is known from [73] that for a viscous compressible vortex the radial pressure distribution given by the solution of

$$\frac{\partial p}{\partial r} = \frac{\rho u_\theta^2}{r}. \tag{34}$$

Assuming a constant temperature distribution $T = T_\infty$, one obtains from (34) the profile

$$P = -P_\infty \frac{C_v^2}{2R_{gas}T_\infty R_v^2} \exp\left(-\frac{r^2}{R_v^2}\right). \tag{35}$$

The maximum radial velocity chosen is $v_{\theta_{max}} = 0.5$ and the vortex radius is $R_v = 0.41$. The simple, undisturbed advection of this vortex was tested successfully for the resolutions employed here in [40, 85]. A reference simulation without vortex was used to calibrate the introduction time, so as to allow the vortex to reach the cylinder at the instant of maximum lift.

To set the values of the adaptation thresholds, as discussed in Section 3, the structure function indicator was evaluated on the velocity field obtained

in a steady state simulation of the cylinder without the vortex with constant $p = 2$. Thresholds were then chosen in order to obtain, for that field, an adapted number of dofs just lower than that of the corresponding number of dofs in the constant $p = 3$ case. The resulting threshold values for the structure function (SF) indicator were then $\epsilon_1 = 5 \times 10^{-4}$, $\epsilon_2 = 10^{-2}$, $\epsilon_3 = 4 \times 10^{-1}$. The dynamical $p-$adaptation strategy consisted in this case of adapting the polynomial degrees approximately three times during the time needed by a fluid particle to pass through the smallest elements on the cylinder walls at the free stream velocity U_∞. This choice led to computing the indicator value at intervals $\Delta t_i = 0.0016$ and averaging them over intervals $\Delta t_a = 0.05$, while the value $\Delta t = 0.0004$ was used for time integration.

The simulations were carried out on the Marconi cluster at CINECA, using 272 Brodwell processors. In Figure 14, the total number of dofs for the adaptive simulations divided by the values for the corresponding constant polynomial degrees are shown as a function of time. As in the case of the mixing layer simulations, the gain in terms of a reduction of the number of DOFs using $p-$adaptivity is evident, since it requires less than 50% of the dofs for the $p = 4$ case and about 40% of the dofs for the $p = 5$ case, with respect to the corresponding constant degree simulations. The core hours necessary to perform the simulations are reported in Table 2. In spite of the absence of a specific dynamic load balancing procedure, the $p-$adaptive technique also yields a reduction of the required CPU time, which has a value only marginally larger than that of the $p = 3$ simulation for the adaptive $p_{max} = 4$, which required 47% of the CPU time of the corresponding constant degree $p = 4$ simulation, while the adaptive $p_{max} = 5$ case required just below 40% of the CPU time of the corresponding constant degree $p = 5$ simulation.

The dynamically adaptive procedure was able also in this case to effectively represent the structures of the flow, both in the advected vortex region and in the wake of the obstacle, as can be seen in Figures 15-17. It is possible to note that a higher polynomial degree is employed in the advected vortex region and in the shear layers around the cylinder. The dynamic adaptation procedure is able

	Core hours	number of degrees of freedom
$p = 5$	1380	1333696
$p = 4$	756	833560
$p = 3$	388	476320
$p-$adaptive $p_{max} = 5$	530	530273 (average)
$p-$adaptive $p_{max} = 4$	462	393854 (average)

Table 5: CPU time required for the vortex-cylinder simulations using uniform polynomial degree distribution $p = 5$, $p = 4$, $p = 3$ and $p-$adaptive simulations with maximum polynomial order equal 4 and 5, respectively. For the $p-$adaptive simulations, the number of degrees of freedom is averaged over the duration of the simulation.

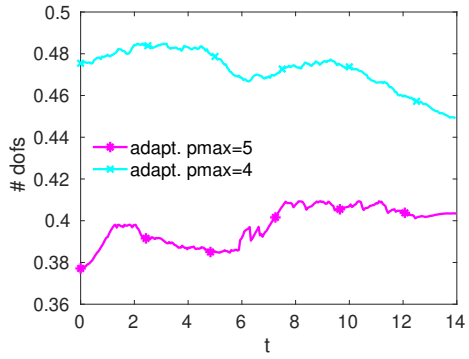

Figure 14: Number of degrees of freedom during the dynamic adaptive simulation of vortex-cylinder interaction, normalised by the number of degree of freedom for the corresponding maximum degree simulation.

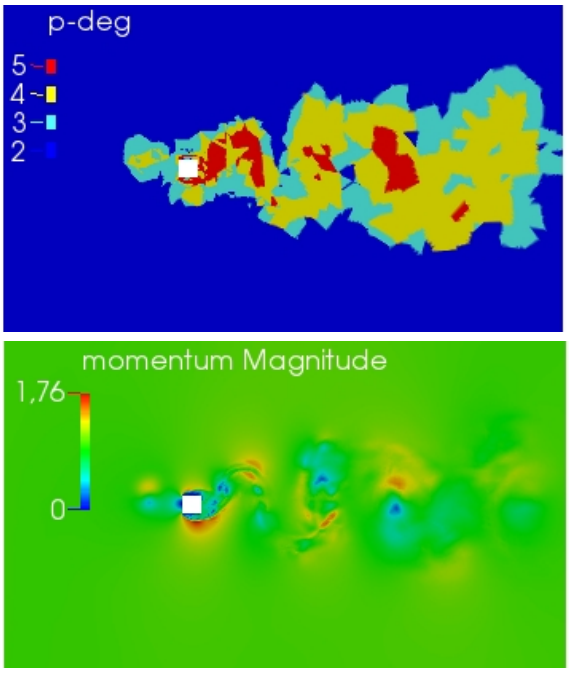

(a)

(b)

Figure 15: Polynomial degree (a) and momentum magnitude fields (b), for the square cylinder–vortex interaction flow at time $t = 4$.

to effectively increase the polynomial degree around the vortex and to follow it as it is advected downstream, leaving all the elements with no vortex activity at the lowest resolution. Notice that the centre of the vortex is represented with polynomials with $p = 4$ in the first instants, but only polynomials with $p = 3$ are employed later, since the vortex enters an area with a more refined mesh in which a lower polynomial degree is sufficient.

Among the different effects caused by the vortex-cylinder interaction, the most interesting are those on the forces acting on the cylinder. In the developed flow around the square cylinder, the periodic oscillations of the force coefficients are related to the unsteadiness of the recirculation bubble on the upper and lower sides and to the vortex shedding. Reaching the upper corner of the cylinder at $t = 5$, the vortex changes the pressure distribution on the front of the cylinder and strongly modifies the recirculating bubble on the upper side.

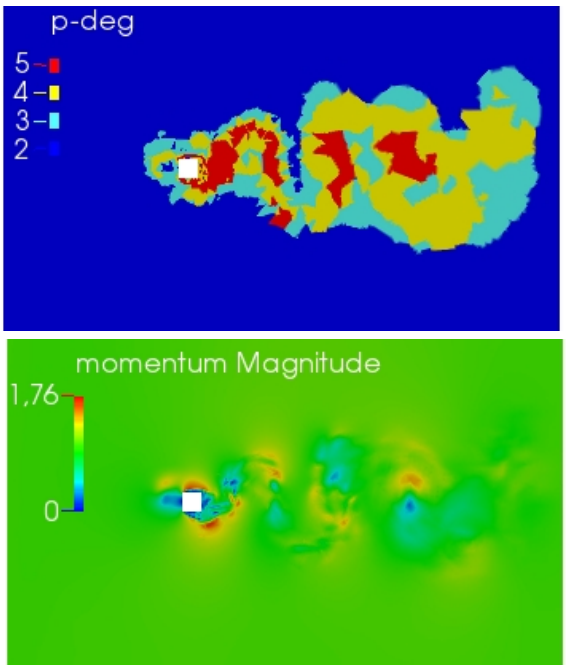

(a)

(b)

Figure 16: Polynomial degree (a) and momentum magnitude fields (b), for the square cylinder–vortex interaction flow at time $t = 5$.

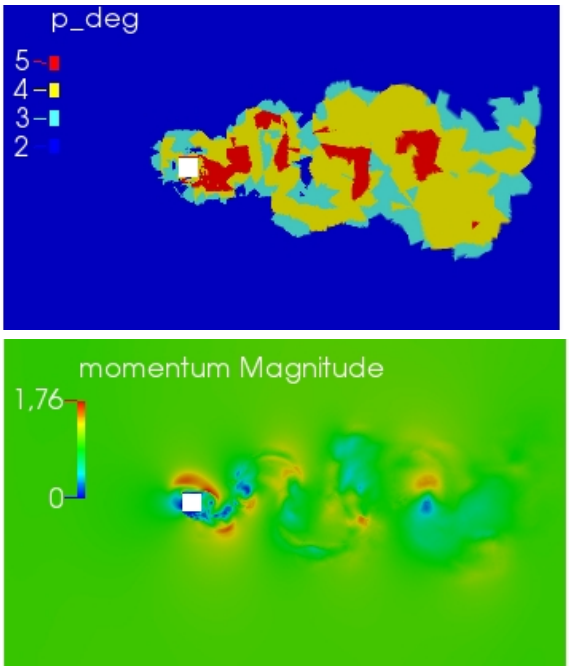

(a)

(b)

Figure 17: Polynomial degree (a) and momentum magnitude fields (b), for the square cylinder–vortex interaction flow at time $t = 6$.

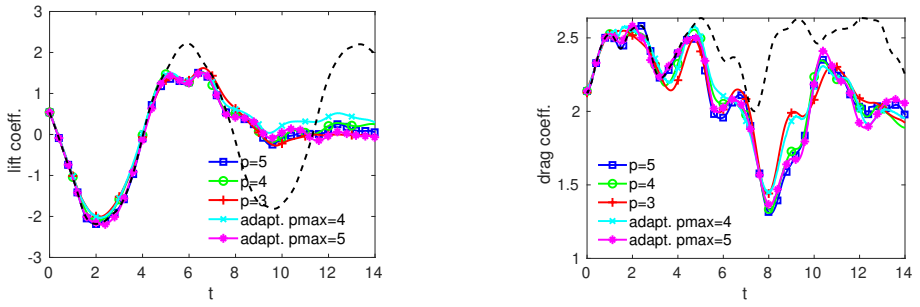

(a) Lift coefficient

(b) Drag coefficient

Figure 18: Force coefficients as a function of time for vortex interacting with the cylinder. The dashed lines represent the reference solution without vortex interaction.

In this condition, it is very important to use an adequate resolution on the upper side and in the separation bubble. The history of the load coefficients before, during and after the interaction is reported in Figure 18. Furthermore, the discrepancies in the maximum an minimum values of the load coefficients with respect to the corresponding no vortex case are also displayed in Table 6.

It can be observed that, up to time $t = 8$, all the simulations yield very similar values for the lift coefficient, while at later times the values obtained with the adaptive $p_{max} = 4$ simulation start to diverge slightly from the others. With respect to the drag coefficient, the adaptive $p_{max} = 4$ simulation is also less on track with respect to the higher resolution simulations, yielding between time $t = 8$ and $t = 10$ values that are closer to those of the constant $p = 3$ degree simulation. On the other hand, on average all simulations yield values that do not diverge more than 10% of the peak values obtained in the reference simulation. A similar behaviour can be observed in the differences of the force coefficients with respect to the simulation without vortex, the adaptive $p_{max} = 4$ simulation yielding values closer to those of the constant $p = 3$ degree simulation, while the adaptive $p_{max} = 5$ simulation is quantitatively in very good agreement with its constant degree counterpart.

configuration	C_L peak diff. %	C_D max diff. %	C_D min diff. %
$p = 5$	-45	-5	-35
$p = 4$	-44	-3	-33
$p = 3$	-43	-6	-28
$p-$adaptive $p_{max} = 5$	-45	-5	-34
$p-$adaptive $p_{max} = 4$	-43	-2	-28

Table 6: Differences, in percentage, of the force coefficients with respect to the simulation without vortex, during the vortex interaction time, $t = 4 - 8.5$. For the lift, only the change in the subsequent peak is presented, for the drag both the difference in maximum and minimum.

6. Conclusion

The need for adaptive LES approaches was first stated in [2], but adaptive LES simulations are not very common yet. DG methods provide an appropriate environment for adaptive approaches, since they do not require to enforce continuity constraints at the inter-element boundaries. Furthermore, $p-$adaptive techniques are appealing, since they allow to correct possible shortcomings of the computational mesh, as well as to perform dynamically adaptive simulations without extensive remeshing.

Static polynomial adaptivity has been applied to LES in a DG context in [44, 13, 38, 40]. An essential tool for $p-$adaptive simulations is an adaptation criterion that, rather than simply increasing the resolution in order to decrease the error, which is known to lead to a DNS solution [31, 30], tries instead to adjust the resolution in order to directly resolve only a prescribed amount of the turbulent scales.

In this work, the physically based refinement indicator proposed by the authors in [13, 40] was shown to be applicable locally and dynamically in time, in order to simulate efficiently and accurately transient phenomena. Numerical simulations of a temporally evolving mixing layer and of a vortex impinging on a square cylinder were performed. The results obtained show that a significant reduction of the computational cost of LES can be achieved, reducing both the

number of degrees of freedom and the CPU time with respect to those required by the corresponding constant maximum polynomial degree simulations. With respect to accuracy, while less reliable for lower values of the maximum allowed polynomial degree, adaptive simulations guarantee in general a level of accuracy equivalent to that of the corresponding constant degree simulations, as long as the maximum allowed polynomial degree is sufficient to resolve well the underlying flow structures.

A major limitation of the present $p-$adaptive strategy is that, in this preliminary implementation of a dynamically adaptive approach, no dynamic load balancing has been performed. In future work aimed at the optimization of our codes, load balancing approaches such as those employed in [36, 65] will be considered and tested in order to achieve maximum parallel efficiency. Furthermore, applications of the proposed $p-$adaptive strategy to more advanced, entropy stable DG methods and more extensive investigations on the procedures for the choice of the threshold parameters are also natural extensions of the work presented here.

Acknowledgements

First of all, we would like to thank two anonymous reviewers for their very constructive criticism, which has helped to improve substantially the first version of this paper. This work presents improvements and further developments of results achieved in the PhD thesis and Master thesis in Aerospace Engineering of two of the authors (M.T, A.R., respectively) at Politecnico di Milano, supervised by the other two authors. This paper benefited from the close collaboration on developing advanced methodologies for heterogeneous high-performance computing platforms within the ESCAPE-2 (No.800897) project funded by the European Union Horizon 2020 future and emerging technologies and the research and innovation programmes. We also acknowledge that the results of this research were made possible by the computational resources made available at CINECA (Italy) by the high performance computing projects ISCRA-C

HP10CHV1QD and ISCRA-C HP10C6F9BK.

References

[1] C. Argyropoulos, N. Markatos, Recent advances on the numerical modelling of turbulent flows, Applied Mathematical Modelling 39 (2015) 693–732.

[2] S. B. Pope, Ten questions concerning the large-eddy simulation of turbulent flows, New Journal of Physics 6 (2004) 35.

[3] F. F. Grinstein, L. G. Margolin, W. J. Rider, Implicit large eddy simulation: computing turbulent fluid dynamics, Cambridge University Press, 2007.

[4] L. G. Margolin, The reality of artificial viscosity, Shock Waves 29 (2019) 27–35.

[5] B. Vreman, B. Geurts, H. Kuerten, Discretization error dominance over subgrid terms in large eddy simulation of compressible shear layers in 2D, Communications in Numerical Methods in Engineering 10 (1994) 785–790.

[6] S. Ghosal, An analysis of numerical errors in large-eddy simulations of turbulence, Journal of Computational Physics 125 (1996) 187–206.

[7] A. Kravchenko, P. Moin, On the effect of numerical errors in large eddy simulations of turbulent flows, Journal of Computational Physics 131 (1997) 310–322.

[8] E. Garnier, M. Mossi, P. Sagaut, P. Comte, M. Deville, On the use of shock-capturing schemes for large-eddy simulation, Journal of Computational Physics 153 (1999) 273–311.

[9] B. Geurts, A. Rouhi, U. Piomelli, Recent progress on reliability assessment of large-eddy simulation, Journal of Fluids and Structures 91 (2019) 102615.

[10] T. Dairay, E. Lamballais, S. Laizet, J. Vassilicos, Numerical dissipation vs. subgrid-scale modelling for large eddy simulation, Journal of Computational Physics 337 (2017) 252–274.

[11] G. Mengaldo, R. Moura, B. Giralda, J. Peiró, S. Sherwin, Spatial eigensolution analysis of discontinuous Galerkin schemes with practical insights for under-resolved computations and implicit LES, Computers & Fluids 169 (2018) 349–364.

[12] G. Mengaldo, D. D. Grazia, R. Moura, S. J. Sherwin, Spatial eigensolution analysis of energy-stable flux reconstruction schemes and influence of the numerical flux on accuracy and robustness, Journal of Computational Physics 358 (2018) 1–20.

[13] M. Tugnoli, A. Abbà, L. Bonaventura, M. Restelli, A locally p-adaptive approach for Large Eddy Simulation of compressible flows in a DG framework, Journal of Computational Physics 349 (2017) 33–58.

[14] L. Demkowicz, J. Oden, W. Rachowicz, O. Hardy, An $h-p$ Taylor-Galerkin finite element method for compressible Euler equations, Computer Methods in Applied Mechanics and Engineering 88 (1991) 363–396.

[15] J. Flaherty, P. Moore, Integrated space-time adaptive hp-refinement methods for parabolic systems., Applied Numerical Mathematics 16 (1995) 317–341.

[16] K. Devine, J. E. Flaherty, Parallel adaptive hp-refinement techniques for conservation laws, Applied Numerical Mathematics 20 (1996) 367–386.

[17] L. Demkowicz, W. Rachowicz, P. Devloo, An fully automatic $h-p$ adaptivity, Journal of Scientific Computing 17 (2002) 117–142.

[18] J. Remacle, J. Flaherty, M. Shephard, An adaptive Discontinuous Galerkin technique with an orthogonal basis applied to compressible flow problems, SIAM Review 45 (2003) 53–72.

[19] P. Houston, E. Süli, A note on the design of hp-adaptive finite element methods for elliptic partial differential equations, Computational methods in applied mechanics and engineering 194 (2005) 229–243.

[20] C. Eskilsson, An *hp*-adaptive discontinuous Galerkin method for shallow water flows, International Journal of Numerical Methods in Fluids 67 (2011) 1605–1623.

[21] G. Tumolo, L. Bonaventura, M. Restelli, A semi-implicit, semi-Lagrangian, p-adaptive Discontinuous Galerkin method for the shallow water equations, Journal of Computational Physics 232 (2013) 46–67.

[22] G. Tumolo, L. Bonaventura, A semi-implicit, semi-Lagrangian, DG framework for adaptive numerical weather prediction, Quarterly Journal of the Royal Meteorological Society 141 (2015) 2582–2601.

[23] G. Tumolo, A mass conservative TR-BDF2 semi-implicit semi-Lagrangian DG discretization of the shallow water equations on general structured meshes of quadrilaterals, Communications in Applied and Industrial Mathematics 7 (2016) 165–190.

[24] N. Chalmers, G.Agbaglah, M.Chrust, C. Mavriplis, A parallel *hp*-adaptive high order discontinuous Galerkin method for the incompressible Navier-Stokes equations, Journal of Computational Physics X 2 (2019) 100023.

[25] A. Burbeau, P. Sagaut, A dynamic $p-$adaptive discontinuous Galerkin method for viscous flow with shocks, Computers & Fluids 34 (2005) 401–417.

[26] O. Antepara, O. Lehmkuhl, J. Chiva, R. Borrell, Parallel adaptive mesh refinement simulation of the flow around a square cylinder at Re = 22000, Procedia Engineering 61 (2013) 246–250.

[27] G. Kuru, M. de la Llave Plata, V. Couaillier, R. Abgrall, F. Coquel, An adaptive Variational Multiscale Discontinuous Galerkin method for Large Eddy Simulation, 54th AIAA Aerosp. Sci. Meet. (2016) 1–10.

[28] J. Wackers, G.Deng, E. Guilmineau, A. Leroyer, P. Queutey, M. Visonneau, Combined refinement criteria for anisotropic grid refinement in free-surface flow simulation, Computers & Fluids 92 (2014) 209–222.

[29] G. Giorgiani, S. Fernández-Méndez, A. Huerta, Hybridizable discontinuous Galerkin with degree adaptivity for the incompressible Navier-Stokes equations, International Journal of Numerical Methods in Fluids 72 (2014) 196–208.

[30] P. Sagaut, Large Eddy Simulation for Incompressible Flows: An Introduction, Springer Verlag, 2006.

[31] S. Mitran, A Comparison of Adaptive Mesh Refinement Approaches for Large Eddy simulations, in: C. Liu (Ed.), Third AFOSR International Conference on Direct Numerical Simulation and Large Eddy Simulation (TAICDL), 2001, pp. 397–408.

[32] J. Hoffman, Computation of Mean Drag for Bluff Body Problems Using Adaptive DNS/LES, SIAM Journal of Scientific Computing 27 (2005) 184–207.

[33] J. Hoffman, C. Johnson, Stability of the dual Navier-Stokes equations and efficient computation of mean output in turbulent flow using adaptive DNS/LES, Computer Methods in Applied Mechanics and Engineering 195 (13-16) (2006) 1709–1721.

[34] J. Hoffman, J. Jansson, R. de Abreu, N. Degirmenci, N. Jansson, K. Müller, M. Nazarov, J. Spühler, Unicorn: Parallel adaptive finite element simulation of turbulent flow and fluid-structure interaction for deforming domains and complex geometry, Computers & Fluids 80 (2013) 310–319.

[35] D. Ekelschot, D. Moxey, S. Sherwin, J. Peiró, A $p-$adaptation method for compressible flow problems using a goal-based error indicator, Computers & Structures 181 (2017) 55–69.

[36] F.Bassi, A. Colombo, A. Crivellini, F. Fidkowski, M. Franciolini, A. Ghidoni, G. Noventa, An entropy-adjoint $p-$adaptive discontinuous Galerkin method for the under-resolved simulation of turbulent flows, in: AIAA AVIATION Forum, 2019.

[37] M. Kompenhans, G. Rubio, E. Ferrer, E.Valero, Comparisons of $p-$adaptation strategies based on truncation-and discretisation-errors for high order discontinuous Galerkin methods, Computers & Fluids 139 (2016) 36–46.

[38] F. Naddei, Adaptive Large Eddy Simulations based on discontinuous Galerkin methods, Ph.D. thesis, Université Paris–Saclay (2019).

[39] F. Naddei, M. de la Llave Plata, V. Couaillier, F. Coquel, A comparison of refinement indicators for $p-$adaptive simulations of steady and unsteady flows using discontinuous Galerkin methods, Journal of Computational Physics 376 (2019) 508–533.

[40] M. Tugnoli, Polynomial Adaptivity for Large Eddy Simulation of Compressible Turbulent Flows, Ph.D. thesis, Politecnico di Milano, Department of Aerospace Science and Technology (2017).

[41] A. Abbà, L. Bonaventura, M.Nini, M. Restelli, Dynamic models for Large Eddy Simulation of compressible flows with a high order DG method, Computers & Fluids 122 (2015) 209–222.

[42] D. Moxey, C. Cantwell, G. Mengaldo, D. Serson, D. Ekelschot, J. Peiró, S. Sherwin, R. Kirby, Towards $p-$adaptive spectral/$h-p$ element methods for modelling industrial flows, in: Spectral and high order methods for partial differential equations ICOSAHOM 2016, Springer, 2017, pp. 63–79.

[43] A. Rueda-Ramírez, G. Rubio, E. Ferrer, E. Valero, Truncation error estimation in the $p-$anisotropic Discontinuous Galerkin spectral element method, Journal of Scientific Computing 78 (2019) 433–466.

[44] M. de la Llave Plata, E. Lamballais, F. Naddei, On the performance of a high-order multiscale DG approach to LES at increasing Reynolds number, Computers & Fluids 194 (2019) 104306.

[45] B. Cockburn, C. Shu, The Runge-Kutta Discontinuous Galerkin method for conservation laws, V, Journal of Computational Physics 141 (1998) 198–224.

[46] R. LeVeque, Finite Volume Methods for Hyperbolic Problems, Cambridge University Press, 2002.

[47] C. Bassi, A. Abbà, L. Bonaventura, L. Valdettaro, Simulation of gravity currents with a high order DG method, Communications in Applied and Industrial Mathematics 8 (2017) 128–148.

[48] G. Mengaldo, D. D. Grazia, D. Moxey, P. Vincent, S. Sherwin, Dealiasing techniques for high-order spectral element methods on regular and irregular grids, Journal of Computational Physics 299 (2015) 56–81.

[49] A. Beck, D. Flad, C. Tonhäuser, G. Gassner, C. Munz, On the influence of polynomial de-aliasing on subgrid scale models, Flow, Turbulence and Combustion 97 (2016) 475–511.

[50] D. Flad, G. Gassner, On the use of kinetic energy preserving dg-schemes for large eddy simulation, Journal of Computational Physics 350 (2017) 782–795.

[51] L. Friedrich, A. R. Winters, D. D. R. Fernández, G. Gassner, M. Parsani, M. Carpenter, An entropy stable h/p non-conforming discontinuous Galerkin method with the summation-by-parts property, Journal of Scientific Computing 77 (2018) 689–725.

[52] L. Friedrich, G. Schnücke, A. R. Winters, D. D. R. Fernández, G. Gassner, M. Carpenter, Entropy stable space–time discontinuous Galerkin schemes with summation-by-parts property for hyperbolic conservation laws, Journal of Scientific Computing 80 (2019) 175–222.

[53] R. Spiteri, S. Ruuth, A New Class of Optimal High-Order Strong-Stability-Preserving Time Discretization Methods, SIAM Journal of Numerical Analysis 40 (2002) 469–491.

[54] S. S. Collis, Discontinuous Galerkin methods for turbulence simulation, in: Proceedings of the 2002 Center for Turbulence Research Summer Program, 2002, pp. 155–167.

[55] S. S. Collis, Y. Chang, The DG/VMS method for unified turbulence simulation, AIAA paper 3124 (2002) 24–27.

[56] F. der Bos, J. van der Vegt, B. Geurts, A multi-scale formulation for compressible turbulent flows suitable for general variational discretization techniques, Computer Methods in Applied Mechanics and Engineering 196 (2007) 2863–2875.

[57] T. Eidson, Numerical simulation of turbulent Rayleigh-Bénard problem using subgrid modeling, Journal of Fluid Mechanics 158 (1985) 245–268.

[58] D. Knight, G. Zhou, N. Okong'o, V.Shukla, Compressible large eddy simulation using unstructured gridss, Tech. Rep. 98-0535, American Institute of Aeronautics and Astronautics (1998).

[59] A. Abbà, C. Cercignani, L. Valdettaro, Analysis of Subgrid Scale Models, Computer & Mathematics with Applications 46 (2003) 521–535.

[60] A. Abbà, D. Campaniello, M. Nini, Filter size definition in anisotropic subgrid models for Large Eddy Simulation on irregular grids, Journal of Turbulence 18 (2017) 589–610.

[61] S. Cerutti, C. Meneveau, Intermittency and relative scaling of subgrid scale energy dissipation in isotropic turbulence, Physics of Fluids 10 (1998) 928–937.

[62] A. Cimarelli, A. Abbà, M. Germano, General formalism for a reduced description and modelling of momentum and energy transfer in turbulence, Journal of Fluid Mechanics 866 (2019) 865–896.

[63] M. Germano, A direct relation between the filtered subgrid stress and the second order structure function, Physics of Fluids 19 (2007) 038102.

[64] S. B. Pope, Turbulent Flows, Cambridge University Press, 2000.

[65] K. Wang, M. Gobbert, M. Yu, A dynamically load-balanced parallel $p-$adaptive implicit high-order flux reconstruction method for under-resolved turbulence simulation, Tech. Rep. arXiv:1910.03693v1, arXiv (2019).

[66] H. Foysi, S. Sarkar, The compressible mixing layer: a LES study, Theoretical and Computational Fluid Dynamics 24 (2010) 565–588.

[67] N. Sandham, W. Reynolds, Three-dimensional simulations of large eddies in the compressible mixing layer, Journal of Fluid Mechanics 224 (1991) 133–158.

[68] B. Vreman, B. Geurts, H. Kuerten, A priori tests of large eddy simulation of the compressible plane mixing layer, Journal of Engineering Mathematics 29 (1995) 299–327.

[69] W. Yang, H. Zhang, C. Chan, W. Lin, Large eddy simulation of mixing layer, Journal of Computational and Applied Mathematics 163 (2004) 311–318.

[70] F. Golansky, V. Fortuné, E. Lamballais, Noise radiated by a non-isothermal, temporal mixing layer. Part II: Prediction using DNS in the framework of low Mach number approximation, Theoretical and Computational Fluid Dynamics 19 (2005) 391–416.

[71] V. Fortuné, E. Lamballais, Y. Gervais, Noise radiated by a non-isothermal, temporal mixing layer. Part I: Direct computation and prediction using compressible DNS, Theoretical and Computational Fluid Dynamics 18 (2004) 61–81.

[72] A. Recanati, Performance analysis of a finite element discontinuous galerkin numerical code for les of a temporal mixing layer., Master's thesis, School of Industrial and Information Engineering, Politecnico di Milano (2019).

[73] T. Colonius, S. Lele, P. Moin, The free compressible vortex, Journal of Fluid Mechanics 230 (1991) 45–73.

[74] M. Tugnoli, A. Abbà, Polynomial Adaptivity in LES: Application to Compressibility Effects Investigation on Bluff Bodies, in: M. Salvetti, V. Armenio, J. Frhlich, B. Geurts, H. Kuerten (Eds.), Direct and Large-Eddy Simulation XI, ERCOFTAC Series, Springer, 2019, pp. 317–323.

[75] D. A. Lyn, S. Einav, W. Rodi, J. Park, A laser-Doppler velocimetry study of ensemble-averaged characteristics of the turbulent near wake of a square cylinder, Journal of Fluid Mechanics 304 (1995) 285–319.

[76] C. Norberg, Flow around rectangular cylinders: Pressure forces and wake frequencies, Journal of Wind Engineering and Industrial Aerodynamics 49 (1993) 187–196.

[77] P. Bearman, E. Obasaju, An experimental study of pressure fluctuations on fixed and oscillating square-section cylinders, Journal of Fluid Mechanics 119 (1982) 297–321.

[78] M. Minguez, R. Pasquetti, E. Serre, Spectral LES of turbulent flows over bluff bodies: from the square cylinder to a car model, in: BBAA VI International Colloquium on: Bluff Bodies Aerodynamics & Applications, 2008.

[79] F. Trias, A. Gorobets, A. Oliva, Turbulent flow around a square cylinder at Reynolds number 22,000: A DNS study, Computers & Fluids 123 (22) (2015) 87–98.

[80] A. Sohankar, L. Davidson, Large Eddy Simulation of flow past a square cylinder: Comparison of different subgrid scale models, Journal of Fluids Engineering, Transactions of the ASME 122 (2000) 39–47.

[81] W. Rodi, Comparison of LESand RANS calculations of the flow around bluff bodies, Journal of Wind Engineering and Industrial Aerodynamics 69–71 (1997) 55–75.

[82] R. Verstappen, E. Veldman, Spectro-consistent discretization of Navier-Stokes : a challenge to RANS and LES, Journal of Engineering Mathematics 34 (1998) 163–179.

[83] P. Voke, Flow Past a Square Cylinder: Test Case LES2, in: J.-P. Chollet, P. R. Voke, L. Kleiser (Eds.), Direct and Large-Eddy Simulation II: Proceedings of the ERCOFTAC Workshop held in Grenoble, France, 16–19 September 1996, Springer Netherlands, 1997, pp. 355–373.

[84] G. Lodato, P. Domingo, L. Vervisch, Three-dimensional boundary conditions for direct and large-eddy simulation of compressible viscous flows, Journal of Computational Physics 227 (10) (2008) 5105–5143.

[85] M. Tugnoli, A. Abbà, L. Bonaventura, Dynamical degree adaptivity for DG-LES models, in: Proceedings of the ICOSAHOM 2018 Conference, 2020.